Aero-structural Analysis of a Deployable Aeroshell in Transonic Flow

Sanjoy Kumar Saha* and Yusuke Takahashi†
Hokkaido University, Kita 13 Nishi 8, Kita-ku, Sapporo, Hokkaido, 060-0808, Japan

The deployable aeroshell, a contemporary reentry system, utilizes a thin flexible membrane surface sustained by pressurized gas to efficiently decelerate a reentry vehicle at high altitudes while enabling low-ballistic-coefficient flight. When an in-flight aerodynamic force is applied, the membrane structure undergoes large deformation that may affect its performance. Hence, a coupled analysis that considers the feedback effect of structural deformation is essential for accurately predicting the behavior of such reentry vehicles. In this study, a numerical framework for coupled aeroelastic analysis was constructed in a partitioned manner using open-source software to elucidate the combined effect of structural deformation and compressible flow dynamics and characterize the aerodynamic performance of reentry vehicles with inflatable structures. The results revealed that the membrane surface was deformed elastically by the aerodynamic force owing to the large difference in pressure distribution between the front and back of the aeroshell. Fluctuating behavior was observed in the aerodynamic coefficients owing to the small-amplitude oscillation of the capsule. This oscillation was induced by the large wake behind the vehicle. Several wrinkles and concave-shaped depressions formed on the membrane surface, which exhibited a circumferential movement tendency with time.

I. Nomenclature

l = length, m
α = angle of attack, °
C_p = pressure coefficient
C_L = lift coefficient
C_D = drag coefficient
C_M = pitching moment coefficient
S = representative area, m^2

Presented as Paper 2023-2109 at the AIAA SciTech Forum, National Harbor, MD, 23–27 January 2023
*Graduate Student, School of Engineering; sanjoysaha@elms.hokudai.ac.jp
†Associate Professor, Faculty of Engineering; ytakahashi@eng.hokudai.ac.jp

dt	=	time step
U_∞	=	free stream velocity, m/s
μ	=	viscosity, Ns/m^2
Re	=	Reynolds number
M	=	Mach number
d	=	aeroshell diameter, m
q_∞	=	dynamic pressure, Pa
ρ	=	density, kg/m^3

II. Introduction

For decades, blunt bodies have been used to safeguard and decelerate space vehicles through the atmospheres of Earth or other planets, as well as to safely return astronauts or scientific samples from the target planets to Earth. As the world embarks on a new era of space exploration and utilization with more complex and diverse mission requirements, investigating different possible concepts and developing innovative decelerator technologies has become important. Various forebody designs have been suggested and investigated to decelerate space vehicles from hypervelocity entry speeds while minimizing the peak heat load the vehicle must sustain. One such design is an inflatable aerodynamic decelerator (IAD), a cutting-edge technology with several advantages, such as deceleration at higher altitudes, reduced aerodynamic heating, low ballistic coefficient flight, higher payload deployment, and mitigation of communication blackout over conventional rigid aeroshell systems. Initially proposed as a spheroid, the IAD eventually transformed into a ballute, a hybrid of a balloon and a parachute. Being inflated before atmospheric entry by the external gas flow, the configuration assumes an aerodynamic shape to use the atmospheric drag force to decelerate the vehicle efficiently. The increased surface area results in a low ballistic coefficient flight, protects the capsule from extreme thermal loads, and reduces the peak values of dynamic pressure. Another possible benefit of such a decelerator is that essential operations such as parachute extraction or retrojet extraction can be dispensed. Thus, a safe, reliable, and cost-efficient decelerator system can be achieved by using inflatable structures.

Over the years, IAD technology has undergone significant research in several sets of system studies, numerical and wind tunnel experiments, and multiple atmospheric flight tests. Space agencies have proposed numerous mission profiles with different aerodynamic shape configurations to develop this technology for use in thin-atmosphere entries and atmospheres of the Earth, Mars, Titan, and gas giants [1–4]. The National Aeronautics and Space Administration (NASA) conducted extensive research on the stacked toroid Hypersonic Inflatable Aerodynamic Decelerator (HIAD) and tension cone Supersonic Inflatable Aerodynamic Decelerator (SIAD) [5–8]. The main benefits of these configurations are their low mass-to-drag producing area ratio, high compactness during launch, and possible avoidance of well-known instabilities in attitude [9]. The Inflatable Reentry and Descent Technology (IRDT) [10] and the Italian Re-entry Nacelle for microgravity Experiments (IRENE) [11] by the European Space Agency (ESA) have studied the development of a deployable capsule for exploring the surface of Mars with a small low-cost lander. An inflatable decelerator system with a flexible membrane was developed by the Japan Aerospace Exploration Agency (JAXA) under the framework of the Membrane Aeroshell for Atmospheric-Entry Capsule (MAAC) [12–14]. The MAAC project focuses on developing inflatable decelerator systems based on a tension cone shape consisting of a capsule, an axisymmetric single-surface membrane created from flexible materials, and an inflatable torus sustained by pressurized gas to maintain its shape. The membrane aeroshell is attached to the inflatable torus at its outer perimeter. The schematic configuration of a reentry system using a thin-membrane aeroshell is shown in Fig. 1.

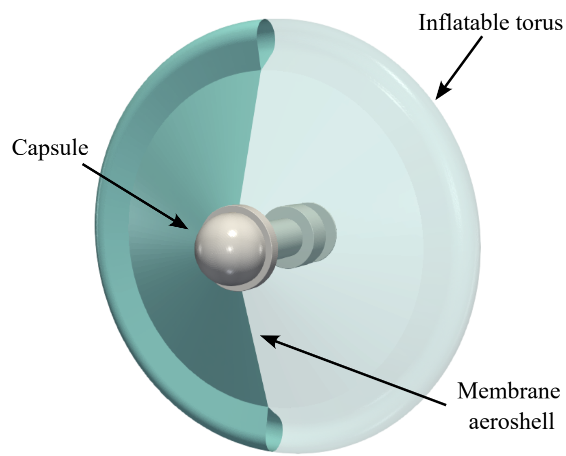

Fig. 1 Schematic of a thin membrane reentry vehicle

To obtain insights into a realizable decelerator with a membrane aeroshell, scholars have utilized elemental studies and flight tests using scientific balloons and sounding rockets under the sounding rocket experiment of the Membrane Aeroshell for Atmospheric-entry Capsule (SMAAC) project [15, 16]. This suborbital flight test aimed to study the feasibility of achieving low-ballistic-coefficient flight and measure the aerodynamic characteristics and attitude behavior. A demonstration test revealed that the attitude of the aeroshell was unstable at subsonic speeds, and the drag coefficient profile exhibited a discrepancy when compared with wind tunnel test results [17, 18]. Owing to the application of modern, lightweight, and flexible materials, IAD surfaces undergo large deformations due to aerodynamic forces. These deformations can change the aerodynamics of the aeroshell. Thus, the accurate characterization of inflatable decelerators requires a coupled analysis to incorporate the combined effects of structural dynamics and compressible flow dynamics. The first studies on developing a coupled analysis algorithm were conducted by Abe et al. [19] and Mosseev et al. [20]. Bartels et al. [21] explored the coupled effects of nonlinear structural dynamics and hypersonic aerothermodynamics by using a loose coupling algorithm. Buck et al. [22] conducted several wind tunnel experimental tests at the NASA

Langley Research Center to develop the capability for testing lightweight flexible materials in hypersonic facilities. Clark et al. [23] conducted the most relevant experimental work to determine the static aerodynamic and aero-elastic characteristics of a scaled semi-rigid and flexible SIAD model in a supersonic wind tunnel. The study revealed the presence of drag hysteresis, in which the structure collapsed at a lower inflation pressure than when it was deployed. Wang et al. [24] conducted a nonlinear structural analysis of a ballute system with wrinkling phenomena coupled with a high-fidelity numerical approach. Kramer et al. [25] investigated the coupled simulation of aerodynamics and structural mechanics for a range of flow conditions and found that the aeroshell exhibits transient oscillatory behavior under impulsive loading, and large nonaxisymmetric oscillations can appear as a result of resonance caused by coupled interaction. Brune et al. [26, 27] performed a detailed uncertainty analysis to predict the deformation and the resulting surface conditions of the HIAD configuration for ballistic and lifting entries.

A high-fidelity computational algorithm for an inflatable decelerator is limited by challenging flow regimes and the difficulty in determining the degree of coupling required for the fluid and structural domains [28, 29]. Some studies have been performed to quantify the structural characteristics and general forms of structural failures of IADs in different configurations by obtaining steady and transient fluid dynamics results [30–33]. Takahashi et al. [34, 35] studied the effects of the structural deformation on the aeroheating characteristics of an SMAAC configuration using one-way coupling. These studies revealed that the shape of a shock wave in the hypersonic region can be changed by structural deformation, thereby affecting the heat load of the aeroshell. A study conducted by Benra et al. [36] revealed that while one-way coupling can only produce plausible results under specific conditions, two-way coupling produces results close to reality. A hypersonic aerothermal study by Dasgupta et al. [37] demonstrated that one-way coupling provided a conservative estimate of aeroheating, which may not be acceptable in some cases. However, a two-way coupled simulation would have generated a more accurate estimate of heating by considering the wall temperature while calculating heat flux. The most recent coupled analysis models, validated by wind tunnel experiments in subsonic regimes, have confirmed the presence of small-amplitude swinging oscillations in combination with membrane deformation [38]. However, the methods developed in these studies require improvements, such as the use of two-way coupling, considering the effects of nonlinear structural factors, and the effects of inflation gas.

This literature survey shows that structural deformation can significantly impact the flow field. Thus, the one-way coupling approach between the flow and structural behavior may cause significant deviations and thereby cannot fully reproduce an actual scenario. Moreover, the aerodynamic force is prominently strong at transonic speeds, and frequent structural failures owing to aero-structural interactions have been observed [39]. The mechanism underlying such a failure is still unknown, and further research into the complex coupled behavior is required because it is critical to the decelerator performance, attitude stability, and precision in landing point determination. Because of the costs of flight tests and data acquisition limitations, numerical simulations are a practical approach for studying the coupled behavior of inflatable decelerators. With the development of large-scale computing resources in recent years, multi-physical problems that can capture the interactions between a flexible decelerator and the flow field can be solved. Considering this background, this study aimed to construct a coupled analysis model based on open-source software to elucidate the combined effect of structural deformation and compressible flow dynamics and characterize the aerodynamic performance of reentry vehicles with inflatable structures under transonic flow speeds.

III. Computational Modeling

The coupled analysis model used in this study was based on open-source fluid solver SU2 [40], computational structural solver CalculiX [41], and the coupling library preCICE [42]. SU2 is a fluid dynamics software for unstructured meshes, and CalculiX is a finite element analysis program for solving structural dynamics. The two solvers are coupled using the preCICE library. An adapter was required for each solver, and it was integrated during the analysis. This section describes the fluid and structural models and the coupling algorithms.

A. Coupling Approach

In multi-physical problems, the strong interaction between each physical phenomenon is crucial for determining the overall response of a system. The coupling method can be categorized as a monolithic or partitioned approach depending on the complexity and interdependence of the physics involved. The monolithic approach addresses both physical fields involved in one solvable system. In contrast, the partitioned approach addresses the physics separately while sharing information to satisfy the requirements of coupled analysis. In this study, we opted for the partitioned approach of coupled simulation because it uses sophisticated algorithms and solvers that have been widely applied and validated. The flow solver SU2 was used to solve the fluid dynamics, and the structural solution was obtained using the structural solver CalculiX. The coupling library preCICE was used to share the solution data between the solvers with the aid of an adapter. The flowchart of this coupling algorithm is depicted in Fig. 2. After the initialization of input parameters such as freestream conditions and grids, SU2 and CalculiX operated in parallel. After one iteration, the solution was shared between the solvers with the aid of the preCICE library. The structural solver passed the displacement data and received the aerodynamic force from the fluid solver. Similarly, the fluid solver sent the aerodynamic force data and received the displacement information of the interface between the fluid and solid domains. The coupled interface used in this study was the membrane surface. Because the number of computational grids was different in the fluid and solid domains, the data for the interface were interpolated using sophisticated data-mapping schemes available in the preCICE library. Nearest-projection data mapping was used in this study for conservative and consistent interpolation of the aerodynamic force and displacement data. Data communication between solvers was managed via TCP/IP sockets. During transient simulation, the fluid domain must be converged to deliver aerodynamic forces on the body within one timestep. By interpolating the forces from the fluid mesh to the structural surface mesh, we obtained a converged solution of the solid domain for the forces from the fluid. After the solution of the solid domain converged, the displacement data were shared with the fluid domain, and the fluid mesh was suitably adapted to accommodate the new surface geometry. This resulted in an internal iteration of the simulation. These steps were continued until the structural displacements and fluid force variations were less than the predetermined values. Subsequently, a new time step was started.

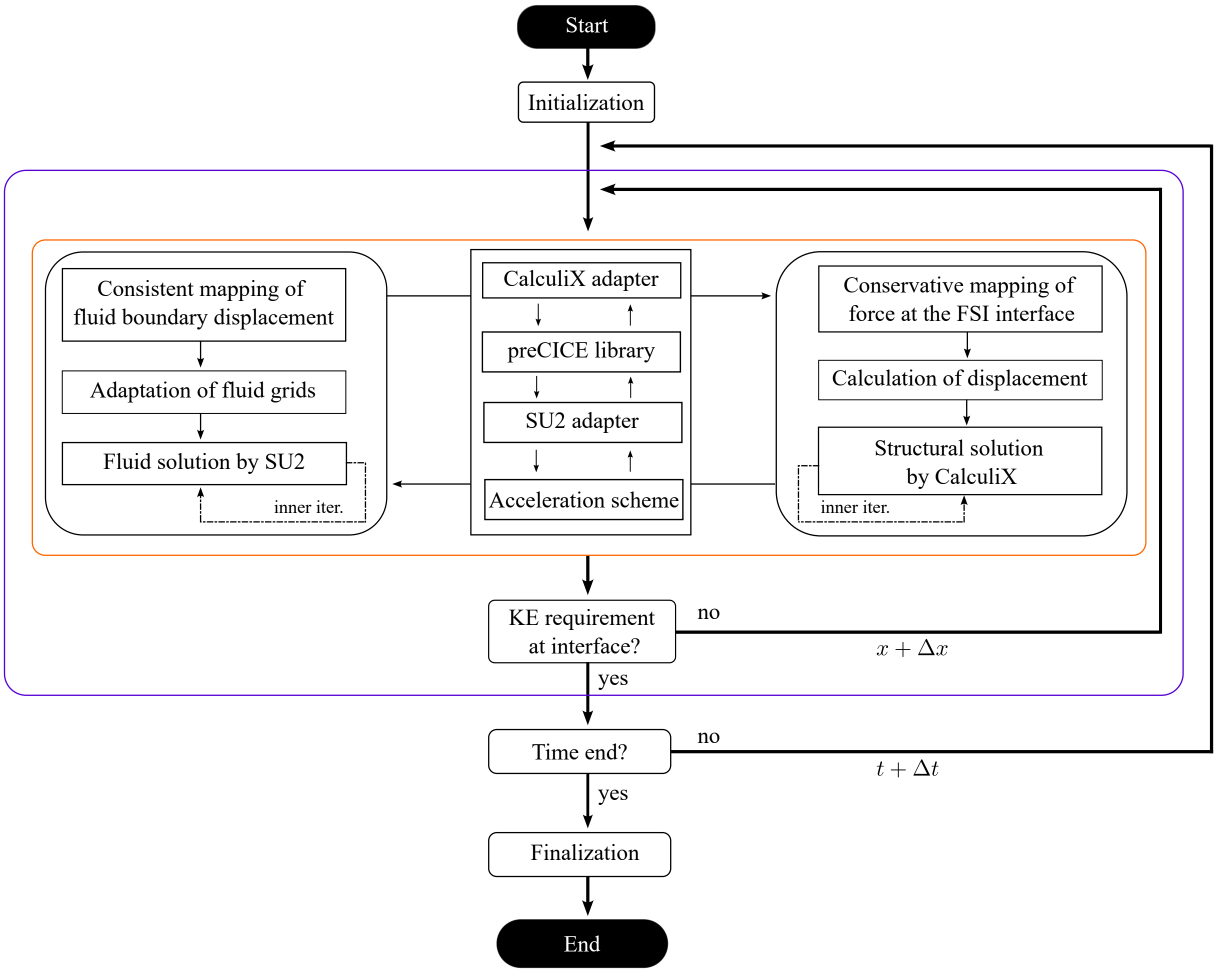

Fig. 2 Flowchart of the coupled model. Here, x: variables transferred by the solvers, t: time, and 'KE': kinematic and equilibrium requirements.

In this study, an implicit coupling scheme was used to satisfy the kinematic and equilibrium conditions at the coupled interface. The quasi-Newton interface [43] relaxation method was adopted to increase the convergence rate, thereby reducing the computational effort. The unsteady fluid and structural domains were solved separately using an iterative staggered approach until the continuity conditions at the interface were satisfied. Thus, two loops existed in the solution scheme: an internal loop to satisfy the kinematic and equilibrium requirements and an external loop to perform time integration.

B. Fluid Model

The governing equations of fluid dynamics are the compressible Navier–Stokes equation and the equation of state for an ideal gas. The Navier–Stokes equation includes the total mass, momentum, and energy conservation laws. The gas was treated as standard air with the same thermodynamic properties at a standard temperature and pressure. The viscosity coefficient of the air was evaluated using Sutherland's formula. The thermal conductivity was evaluated using the viscosity coefficient, the specific heat at constant pressure, and a Prandtl number of 0.72. The governing equations were discretized into finite volumes to perform the unsteady calculations. The spatial gradients of the flow properties were calculated using the Green–Gauss method. The advection fluxes in the governing equations were estimated using the Jameson—Schmidt—Turkel (JST) scheme [44]. artificial dissipation coefficients of 0.5 and 0.02 were used for the second and fourth orders, respectively. Viscosity fluxes were evaluated as the average values of the spatial gradients of the flow parameters between adjacent cells. Time integration was performed implicitly using dual-time stepping. The FGMRES method, which incorporates the lower-upper symmetric Gauss–Seidel (LU-SGS) implicit relaxation method as a preprocessing step, was selected as the matrix solution method. The software suite SU2 was used to solve the unsteady flow. The SU2 suite is a well-established open-source platform for computational fluid flow analysis and aerodynamic shape optimization problems on general unstructured meshes based on the finite volume method. The version of SU2 was SU2-v6.0.0 ('Falcon'), and all explanations are limited to this version. SU2 can be executed in an intrafield-parallel manner such that the computational domain can be split into several parts, enabling large-scale simulations in a feasible time. In this study, parallel computation was performed using the domain decomposition method, and communication was managed via a message-passing interface (MPI). Domain decomposition was performed using ParMETIS, a standard parallel method for fluid flow calculations on a wide range of computers. An adapter, which is a glue code that enables SU2 to communicate with the preCICE library, was used for data communication between the solvers. A grid deformation scheme was implemented to stably deform the computational grids and accommodate the interface deformation. The proposed scheme does not incorporate any turbulence model.

C. Structural Model

Because the membrane surface is very flexible, the deformed configuration of the reentry vehicle differ significantly from that of the undeformed one. The accurate modeling of structural dynamics is essential to properly assessing the combined effects of structural deformation and compressible flow dynamics. In this study, the analysis object was considered a three-dimensional continuum, and the temperature changes inside the object were not considered. In the finite element formulation, the governing equation of structural dynamics was based on the principle of virtual work. This equation comprises the displacements of each element, element stiffness matrix, element load vector, and element mass matrix. The body was discretized into a finite number of microelements. The finite element analysis software CalculiX v2.15 was used as the transient structural solver. A three-dimensional 10-node tetrahedral quadratic

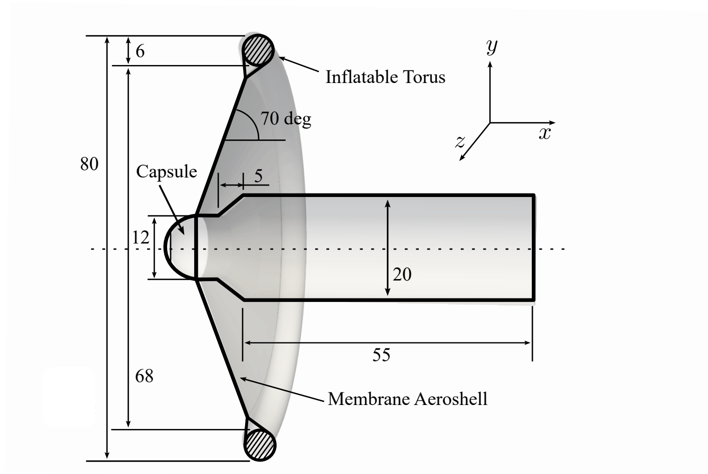

(All dimensions are in mm)

Fig. 3   Geometry of the aeroshell model

element was used to discretize the object. The load vector, stiffness matrix, and mass matrix were calculated for each element. Numerical integration of each element was required to obtain the load vector, stiffness matrix, and mass matrix. The Gauss–Legendre quadrature integral was adopted using the α-method [45] to solve the overall stiffness equation. The α-method uses the parameter $\alpha \in$ [-1/3, 0] and is second-order accurate and unconditionally stable. In this case, the value of α was set to -1/3. The analysis was performed in a geometrically nonlinear mode to accommodate large deformations, which required iterative calculations and increased computational complexity. Parallel computations of the structural solution were performed through thread parallelism using OpenMP. An adapter was used in CalculiX to communicate the data between solvers via the preCICE library. The material properties were assumed to be linear.

IV. Research Object

The research object of this study was a subscale model that imitates an actual deployable aeroshell. The geometric configuration is shown in Fig.3. The model was composed of a blunt hemispherical capsule, a membrane surface created from the flexible material ZYLON [46], and an inflatable torus to maintain the shape of the aeroshell as shown in Fig. 4. ZYLON is a heat-resistant high-strength fabric with potential applications in reentry vehicles. The maximum diameter of the model was 80 mm, and the flare angle was 70°. The inflatable torus frame had a tube diameter of 6 mm, and the thickness of the membrane surface was 0.15 mm. We assumed that the inflatable torus was sufficiently pressurized; therefore, inflation systems were not included in this study. The connection between the capsule and membrane surface was fixed. Additionally, a sting was modeled to replicate the conditions of the wind tunnel analysis, which is a future study.

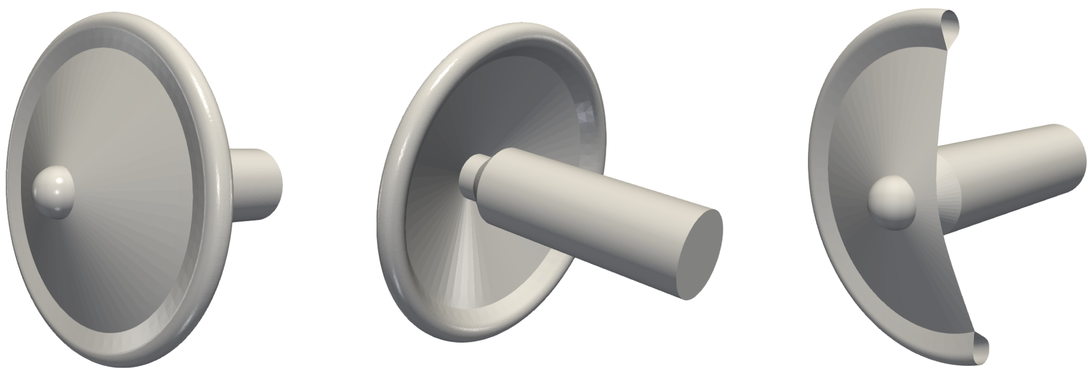

(a) Front view **(b) Back side view** **(c) Sectional view**

Fig. 4 Model for numerical analysis

V. Calculation Conditions and Convergence Studies

A. Calculation Conditions

For the coupled analysis, the aeroshell was placed in freestream flow. Freestream parameters, such as freestream pressure, density, Mach number, and temperature, were determined from the equation of the isentropic process and were given as freestream conditions. In this study, the Mach number was changed between 0.9, 1.1, and 1.2, and the reservoir pressure and temperature were 150 kPa and 250.9 K, respectively. The angle of attack was varied between 0°, 10°, 20°, and 30°. The Reynolds number was of the order of 10^5 for a characteristic length of 0.08 m, as summarized in Table 1. The number of computational nodes for the flow simulation was 5,231,841. The computational grids used for the flow simulations are shown in Fig. 5(a). The time step for the fluid flow analysis was 1.0×10^{-4} s/step. The dynamic pressure of the flow was 7.95 kPa. With a gas constant of 287.058 J/kg.K and specific heat ratio of 1.4, we expected that the air would satisfy the equation of state. The computational mesh used for structural simulation is shown in Fig. 5(b). The mesh consisted of tetrahedral grids. The number of grids was 65,011. The capsule and sting were set as fixed boundaries. The remaining were free boundaries and coupled interfaces. The membrane surface was modeled as a ZYLON fiber, and the material properties used for the structural analysis were the same. Young's modulus of the ZYLON fiber was set to 700 MPa, Poisson's ratio to 0.3, and the density to 900 kg/m^3. In a coupled simulation, replicating the actual anisotropy and nonlinear material properties is difficult. Therefore, as a first step, the material nonlinearity was not considered in this study, although the geometric nonlinearity was used to accommodate large deformations. The time step for the structural analysis was 1.0×10^{-4} s/step.

The computational domain of the flow simulation is shown in Fig. 6. This figure shows the boundary names for each boundary condition. The analysis domain was a coordinate system with the origin at the tip of the aeroshell $(x, y, z) = (0, 0, 0)$. The inlet was a freestream boundary. A zero-gradient condition was applied at the outlet for all flow properties. The membrane surface was assumed to be at a constant temperature of 300 K, and a no-slip condition

Table 1 Calculation conditions for fluid flow

M_∞	p_∞, kPa	Re_∞	μ_∞, Nsm^{-2}
0.9	150	7.049×10^5	1.637×10^{-5}
1.1	150	6.644×10^5	1.595×10^{-5}
1.2	150	6.170×10^5	1.579×10^{-5}

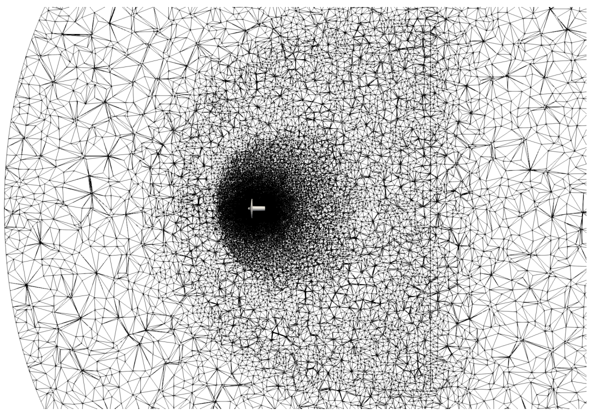

(a) SU2 mesh

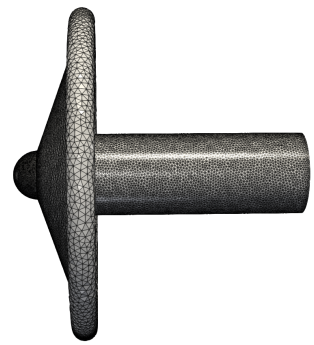

(b) CalculiX mesh

Fig. 5 Computational mesh for flow and structural analysis

was used.

B. Convergence Studies

1. Mesh Convergence Study

To ensure that the solutions obtained by the coupled model were invariant to the refinement of the computational grids, we conducted a grid study for Mach numbers of 0.9 and 1.2, maintaining the angle of attack at 0°. Five fluid meshes were studied with increasing levels of refinement: one coarse, three intermediate, and one fine. These grids were studied for a Mach number of 0.9 to compare the average drag coefficient values. The drag coefficient was selected as the quantity for the convergence study because it is crucial for characterizing the performance of the aeroshell as an aero-decelerator. As shown in Fig. 7(a), for the fluid flow analysis, a maximum difference of about 0.58% was observed between the coarse and intermediate meshes, and for other meshes, it was below 0.3%. Therefore, all intermediate meshes were sufficient for the computations. However, for fluid flow analysis, 5,231,841 grids were selected because they were more compatible with the selected structural mesh and enabled faster FSI calculation. Four different structural meshes with increasing levels of refinement were studied: one coarse, two intermediate, and one fine, as shown in Fig. 7(b). These grids were studied for a Mach number of 1.2 to compare the maximum value of the torus displacement. The differences between the maximum displacement values were 14.44%, 2.67%, and 2.72%. Because the differences were less than 5%, we selected a mesh with 65,011 grid points for the analysis.

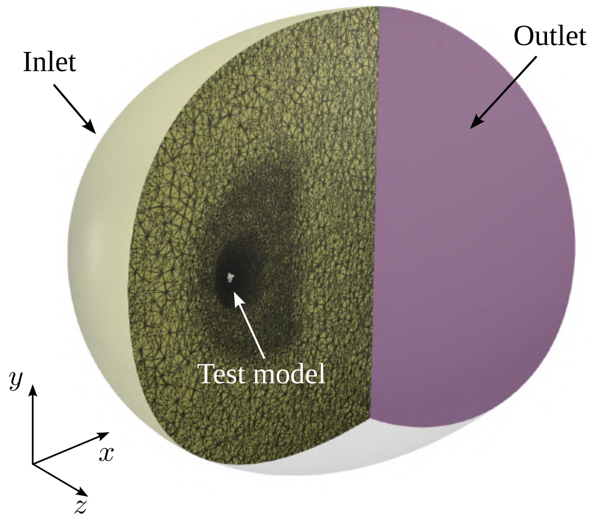

Fig. 6 Computational domain

2. Timestep Convergence

To investigate the impact of timestep size on the accuracy of the results, we conducted a timestep study by varying the size of the timesteps. Timestep sizes of 2×10^{-4}, 1×10^{-4}, and 5×10^{-5} were studied for a Mach number of 1.2 with no angle of attack, and the results demonstrated that the choice of timestep has a considerable impact on the temporal resolution of the simulation. Similar to the mesh convergence study, the drag coefficient and maximum structural deformation were selected as the convergence criteria because they are the primary performance metrics for a deployable aeroshell. A comparison between the drag coefficient and maximum structural deformation is shown in Table 2. Between the 1×10^{-4} and 5×10^{-5} cases, both the drag coefficient and maximum deformation variance were below 5%. Therefore, a timestep size of 1×10^{-4} was selected for this study. Thus, the selected timestep size was reliably balanced between accuracy and computational efficiency.

Table 2 Comparison of parameters for timestep study

dt, s	C_D	Max. Displacement, mm
2×10^{-4}	1.4875	0.4779
1×10^{-4}	1.4596	0.1835
5×10^{-5}	1.4613	0.1865

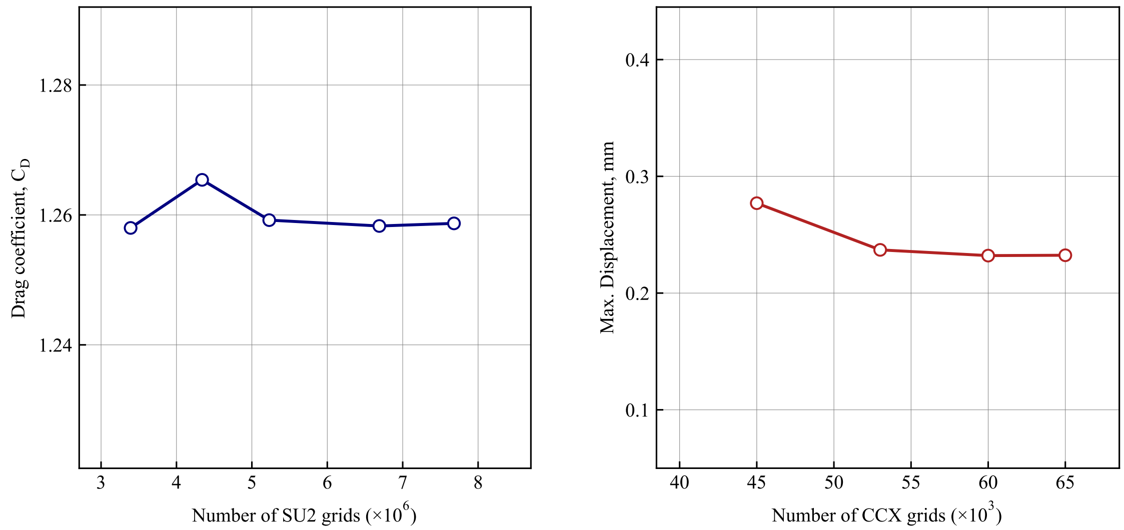

(a) Fluid grid study (fixed CCX grids) **(b) Structural grid study (fixed SU2 grids)**

Fig. 7 Grid dependency study

VI. Results and Discussion

This section first describes the natural modes of oscillation and their respective frequencies through numerical analysis of the scaled model of the deployable aeroshell. The results of the rigid-model analysis are discussed to investigate the interdependence and complexity of the physics involved. Finally, the results of the coupled analysis are compared with those of the rigid model. To analyze the results, we describe the aerodynamic coefficients as follows:

$$C_D = \frac{D}{q_\infty S} \tag{1}$$

$$C_L = \frac{L}{q_\infty S} \tag{2}$$

$$C_M = \frac{M}{q_\infty S l} \tag{3}$$

where q_∞ denotes the dynamic pressure of the freestream, and S is the characteristic area corresponding to the frontal projected area of the aeroshell. In addition, D, L, M, and l are the drag force, lift force, pitching moment, and characteristic length (0.08 m), respectively. The pitching moment was defined around the y-axis, with the head-up as positive and the center of moment coinciding with the center of gravity at $(x, y, z) = (0.01, 0.0, 0.0)$ m.

A. Natural Oscillation Modes

Knowledge of the free oscillations of systems is essential when designing space vehicles because they describe the linear dynamic characteristics of a vehicle without the action of aerodynamic loads and depend only on the inherent properties of the system. The main objective is to avoid adverse effects resulting from structural resonance, a phenomenon that produces high stresses and forces and undesirable structural damage when the frequency range of dynamic loads coincides with natural frequencies. Therefore, the natural frequencies and associated mode shapes of the membrane aeroshell were investigated in this study using the finite element solver CalculiX. The eigenfrequency and eigenmodes were obtained by solving the following equation:

$$Kx = \lambda Mx \tag{4}$$

where K, M, x, and λ are the overall stiffness matrix, mass matrix, eigenvector, and eigenvalue, respectively. Table 3 lists the natural frequencies of the first ten modes. The first to sixth natural oscillation modes are shown in Fig. 8, and the seventh to the tenth modes are omitted. The first and second modes are the pitching and yawing oscillations, respectively. The third mode is torsional bending, in which the membrane surface twists about the x-axis. The fourth mode is the first-order translation mode in the x direction, often called axial deformation, and the fifth mode is the first-order bending mode. For the analysis conditions in this study, a combination of the first and fifth modes appeared, excluding the third mode.

Table 3 Natural modes of oscillation and frequencies

Mode	Frequency, Hz
1	59.3
2	59.3
3	210.5
4	365.1
5	383.2
6	383.2
7	791.7
8	791.8
9	793.6
10	830.6

B. Rigid Model Analysis

To investigate the fundamental features of the transonic compressible flow around an aeroshell, we performed a numerical analysis considering the model as a rigid body. As representative examples, Figs. 9(a) and 9(b) show the instantaneous distributions of the Mach number and pressure coefficient for M1.1 without the membrane deformation. A strong bow shock wave was generated for Mach numbers 1.1 and 1.2 in the windward area. No shock waves appeared for Mach number 0.9. The incoming high-speed flow stagnated in front of the capsule; therefore, a high-pressure region

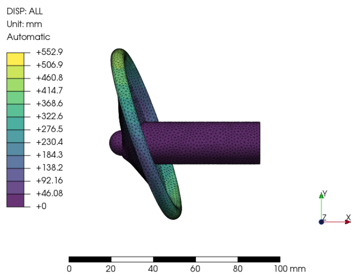

(a) First mode

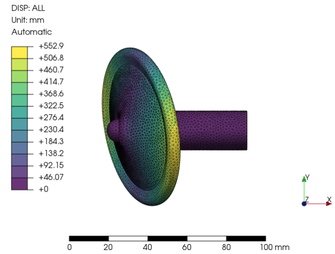

(b) Second mode

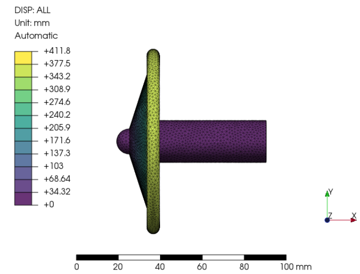

(c) Third mode

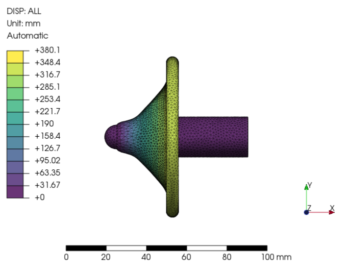

(d) Fourth mode

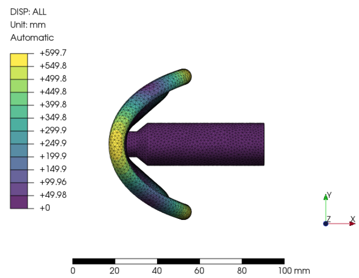

(e) Fifth mode

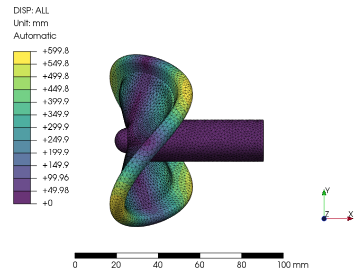

(f) Sixth mode

Fig. 8 Natural modes of oscillation for MAAC

appeared in the front, and a low-pressure region formed at the rear side of the aeroshell. Flow separation occurred near the torus and was accompanied by expansion waves. Alternating vortices and thin shear layers formed in the large recirculation region behind the aeroshell. For inflatable reentry vehicles, the pressure component of the aerodynamic forces, including moments, was significantly greater than that of the friction component. This was primarily because the front stagnation and wake created large differences in the pressure distribution between the front and rear sides.

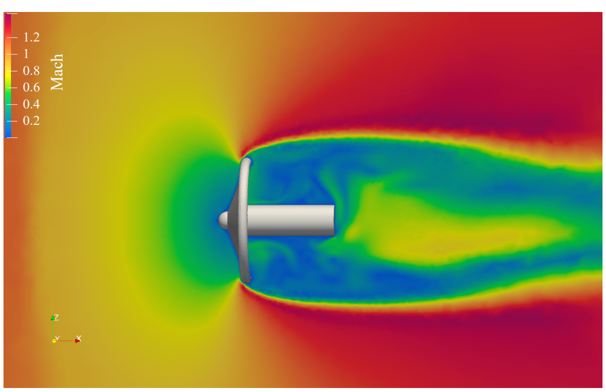

(a) Mach number

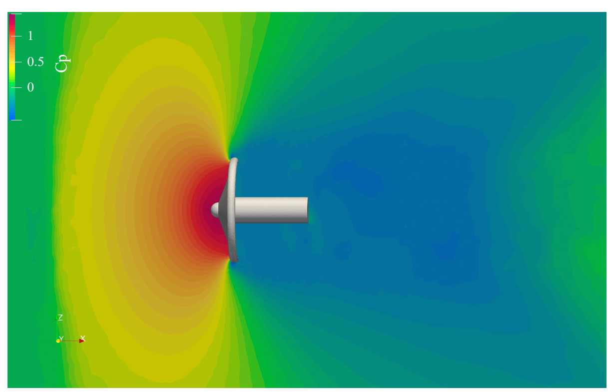

(b) Pressure coefficient

Fig. 9 Distribution of intantaneous flow parameters for freestream Mach 1.1

C. Elastic Deformation and Flow Field

Aerodynamic behavior considering the effect of structural deformation is essential for characterizing the performance of a deployable aeroshell. From an aerodynamic perspective, the pitching moment is a crucial parameter because it is related to attitude instability, which is a major concern in the development of innovative decelerator technology. Similarly, the drag coefficient is another parameter that determines the performance of an aeroshell as an aero-decelerator. A comparison between the pitching moment and drag coefficient for the rigid and elastic model analyses at different angles of attack is shown in Fig. 10. We observed that the value of the pitching moment coefficient was relatively small and nearly zero for the angle of attack of 0°. As the angle of attack increased, the pitching moment coefficient values tended to increased negatively. Generally, the closer the pitching moment was to a positive value, the more unstable the attitude. From this perspective, we can concluded that the aeroshell are statically stable in attitude. The fluctuating behavior observed in the time history data of the pitching moment coefficient was caused by the small-amplitude oscillation of the capsule observed in the elastic simulation. As shown in Fig. 10(d), the drag coefficient values for rigid and elastic model analysis closely matched. However, some differences were observed at the angles of attack of 10° and 20° for Mach numbers of 1.1 and 1.2. Therefore, we inferred that the deformation of the membrane surface may have minimal influence on the performance of the aeroshell as an aero-decelerator under the selected flow conditions.

The Mach number distributions from the coupled analysis for different angles of attack and Mach numbers are shown in Fig. 11. For α = 10°, the wake behind the aeroshell was larger than that for α= 0°. The amplitude of oscillation of the aeroshell was low. However, when α = 20°, the flow field was significantly asymmetric and large oscillations were observed. With a further increase in α= 30°, the wake behind the aeroshell became more prominent, and the wake width exceeded the diameter of the aeroshell. The front shock wave tended to oscillate as the aeroshell oscillated under the aerodynamic loads. In the recirculation region, a reverse flow toward the flexible aeroshell occurred, but the aerodynamic force acting on the rear of the aeroshell was weaker than that acting on the front because of the decrease in density caused by the expansion.

The deformed shape of the membrane aeroshell is shown in Fig. 12. The aeroshell was deformed under the action of aerodynamic force. The maximum displacement of the membrane surface was approximately 2% of the maximum diameter of the aeroshell at a uniform flow Mach number of 0.9. The average displacement was approximately 0.12–0.24 mm. Wrinkles were formed on the aeroshell which exhibited a circumferential movement tendency with time. For Mach 0.9, several secondary depressions that dissipated into larger prominent symmetric depressions over time were initially observed. For α = 10°, a larger depression was formed in the lower half of the aeroshell than in the upper half. When α = 20°, the depression was larger than when α = 10°. The average displacement was greater for an angle of attack of 10°, and a decreasing trend was observed with a further increase in the angle of attack, owing to the asymmetric nature of the incoming flow. The maximum displacements normalized by the diameter of the aeroshell are listed in Table 4.

As a result of membrane deformation, a change in the shock standoff distance was observed at Mach 1.1 and 1.2.

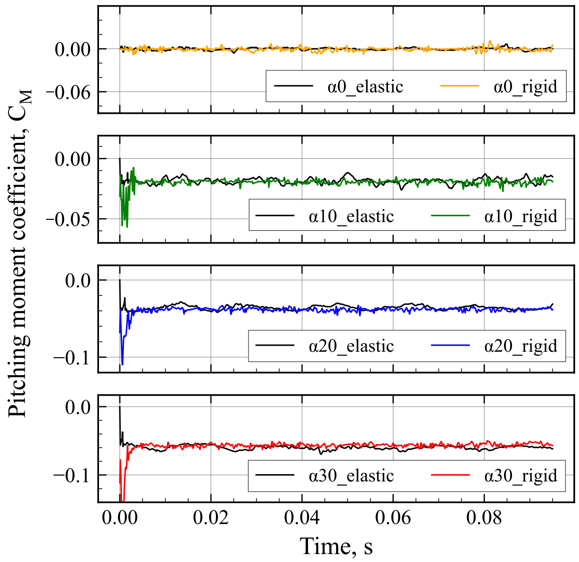

(a) Mach 0.9

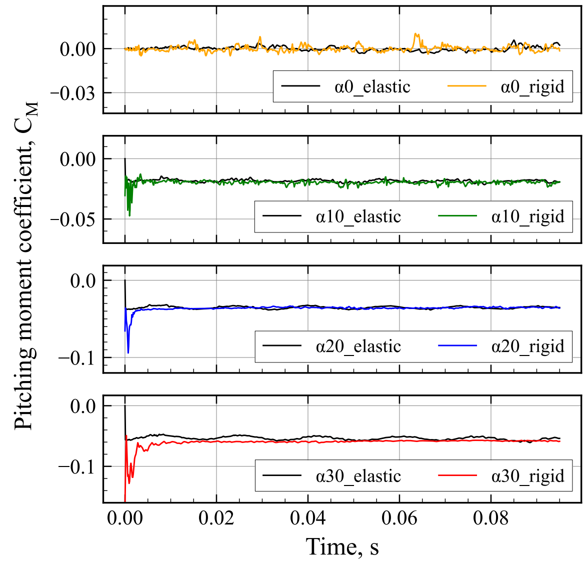

(b) Mach 1.1

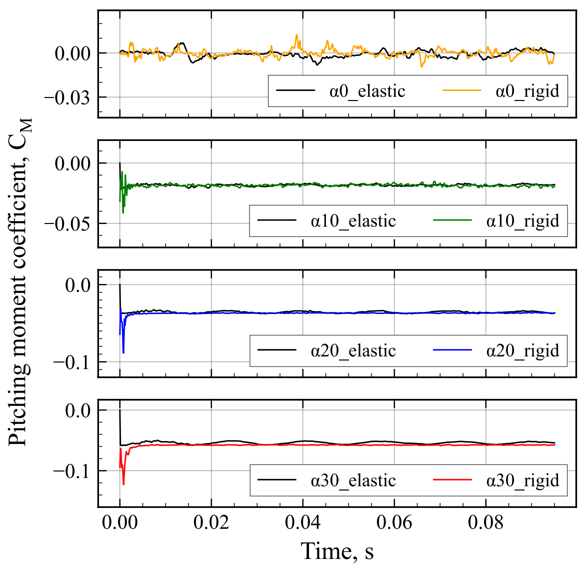

(c) Mach 1.2

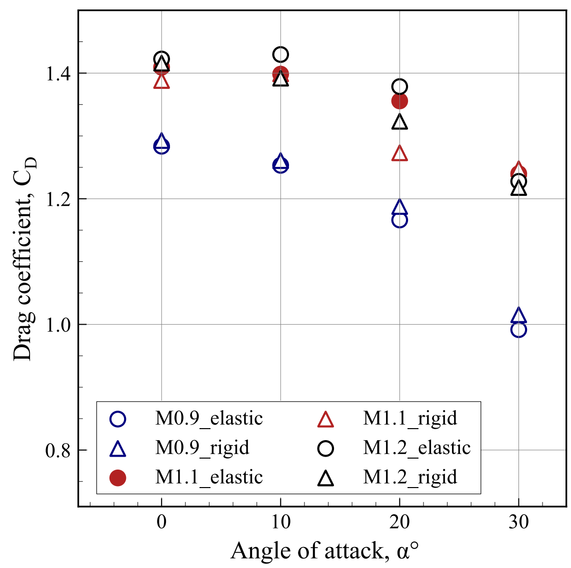

(d) Drag coefficient

Fig. 10 Comparison between the pitching moment and drag coefficient for rigid and elastic model analysis

Owing to the aerodynamic force acting on the membrane surface, it was elongated, thereby decreasing the effective flare angle. When the results of the rigid and elastic model analyses were compared, the shock wave was observed to have shifted toward the aeroshell. This movement was approximately 5.2% relative to the diameter of the aeroshell of 80 mm owing to the effect of membrane deformation, as shown in Fig. 13 schematically. Additionally, when the Mach number of the incoming flow decreased from 1.2 to 0.9, a shift in the flow separation point was observed. The separation point moved forward with a decrease in the Mach number, as shown in Fig. 14, resulting in a decreased drag coefficient.

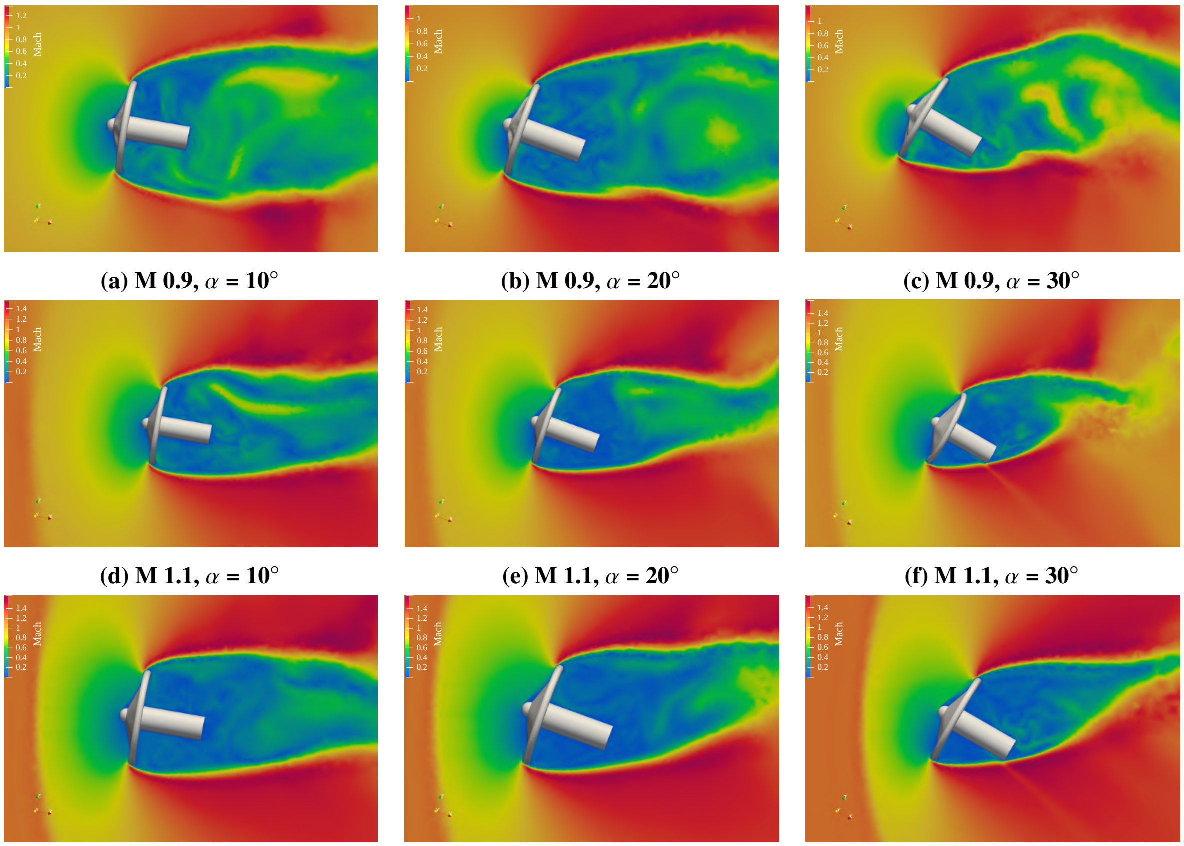

(a) M 0.9, α = 10° (b) M 0.9, α = 20° (c) M 0.9, α = 30°

(d) M 1.1, α = 10° (e) M 1.1, α = 20° (f) M 1.1, α = 30°

(g) M 1.2, α = 10° (h) M 1.2, α = 20° (i) M 1.2, α = 30°

Fig. 11 Instantaneous Mach number distribution for various cases

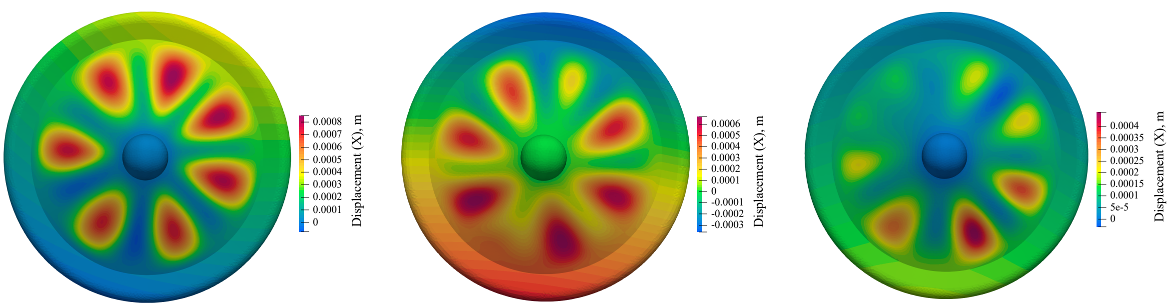

(a) M 0.9, α = 0° (b) M 1.1, α = 10° (c) M 1.2, α = 30°

Fig. 12 Displacement of the membrane aeroshell

D. Oscillation Behavior

To measure the oscillatory behavior of the aeroshell using the coupled analysis model, we adopted the probe technique. Two probe points were selected on the structural mesh at the upper and lower halves of the aeroshell to measure the displacement data in the x direction and all aerodynamic coefficients. The locations of the probe points are shown in Fig. 15. Subsequently, a fast Fourier transform (FFT) was used to determine the frequency spectrum of the oscillations from the torus displacement data. The frequency-domain plots of the inflatable torus displacement

Table 4 Maximum deformation of the membrane

Mach	α, °	Max. Disp., %d
0.9	20	2.02
0.9	0	1.59
0.9	10	1.24
0.9	30	1.21
1.1	30	0.97
1.2	30	0.92
1.1	20	0.84

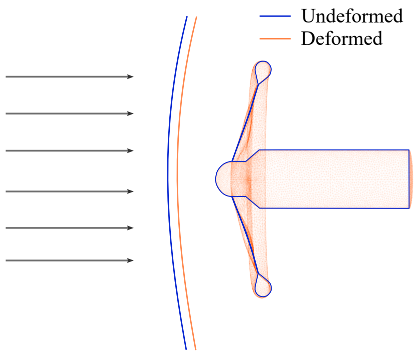

Fig. 13 Shock position

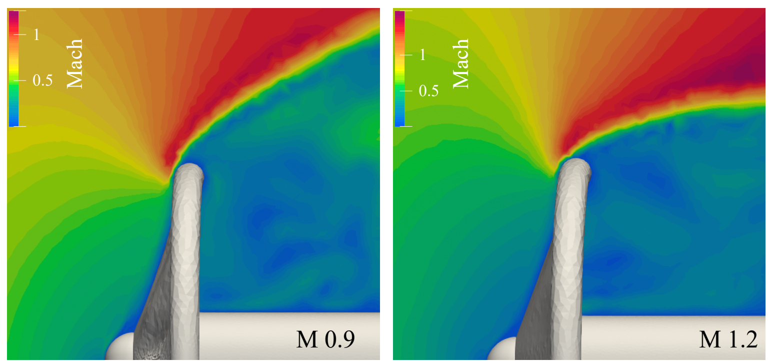

Fig. 14 Separation point shift

and pitching moment coefficients are shown in Figs. 16 and 17, respectively. Because both probe points had similar time history data, these plots were based on the data obtained from the lower probe point (P2). Generally, two peaks appeared in the frequency plots of the torus displacement, and one peak appeared for the pitching moment coefficient.

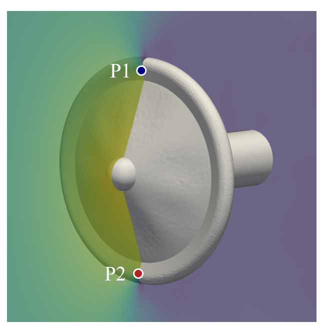

Fig. 15 Location of the probe points

The peak oscillation frequency for the inflatable torus displacement varied arbitrarily depending on the Mach number of the flow. For freestream Mach 0.9, the peak frequency was 63 Hz for all angles of attack, except at 10°. Because this oscillation frequency did not correspond to the natural oscillation frequency, we inferred that this oscillation was caused by the interaction between the aerodynamic forces and moments. For α = 10 °, the peak frequency was 327 Hz, but

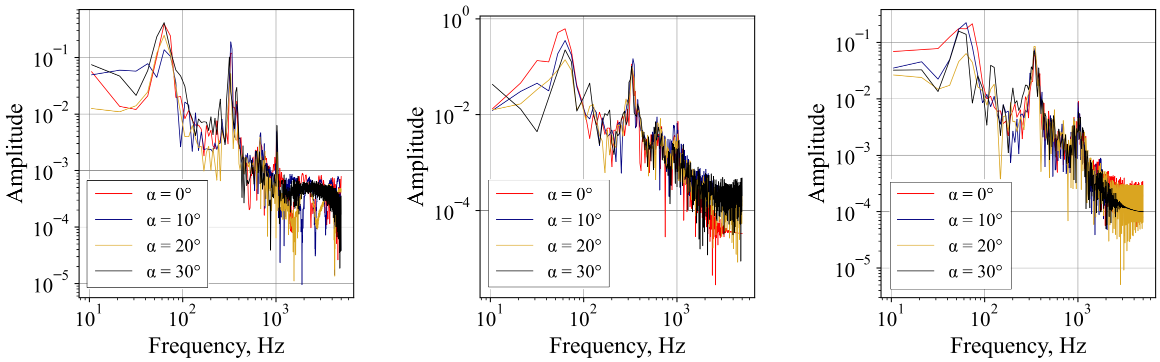

(a) Mach 0.9 **(b) Mach 1.1** **(c) Mach 1.2**

Fig. 16 Frequency-domain plot of torus displacement

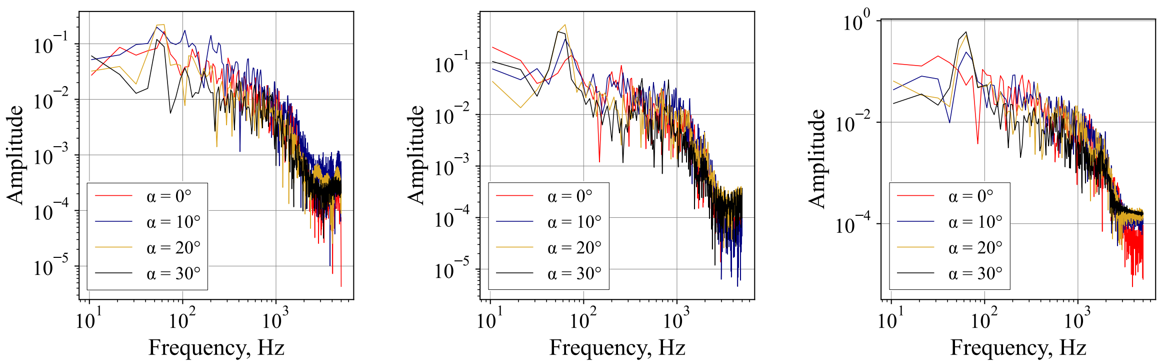

(a) Mach 0.9 **(b) Mach 1.1** **(c) Mach 1.2**

Fig. 17 Frequency-domain plot of pitching moment coefficient

the amplitude was smaller than that in the other cases. The oscillation frequency of the pitching moment coefficient was 52–63 Hz for all the angles of attack. When the freestream Mach number was 1.1, the peak frequency of torus displacement was 63 Hz for all angles of attack. However, the pitching moment coefficient frequency exhibited a decreasing trend with an increase in the angle of attack. For Mach 1.2, the peak frequency of the torus displacement was 52–73 Hz for all angles of attack except at 20°. The peak frequency was 337 Hz with a very small amplitude. The frequency of the pitching moment coefficient was 31 Hz only for $\alpha = 0\,^\circ$ and 63 Hz for all other angles of attack. We consider that a relationship may exist between these oscillation frequencies and the flow's dynamic pressure. In future research, the effect of dynamic pressure on the oscillatory behavior will be investigated, and the dominant oscillation modes will be identified. Additionally, in this study, membrane deformations were primarily influenced by the pressure component of the aerodynamic forces, making turbulence effects secondary and justifying the use of a laminar model to reduce computational costs. In the future, a coupled analysis with a turbulent model will be necessary to accurately capture the impact of turbulence on the aero-structural behavior of the membrane aeroshell.

E. Parameter Study

1. Effect of Young's Modulus

Young's modulus, defined as the ratio of stress to strain, is a metric used to determine the stiffness of an elastic material. The membrane material, ZYLON, is deformable and exhibits nonlinear behavior, which should be considered to accurately predict the performance of this type of space vehicle. However, modeling such nonlinear characteristics in coupled analysis can be complicated and can affect the stability of the solution. Therefore, in this study, the effect of Young's modulus on aerodynamics and structural deformation was investigated. A numerical analysis considering structural deformation was performed for three different values of Young's modulus: 700, 1000, and 1200 MPa. These values were selected arbitrarily based on tensile test data of ZYLON. The freestream Mach number for all three cases was 1.2 with no angle of attack. The obtained results showed that Young's modulus may have a low influence on the aerodynamics of the membrane aeroshell. As shown in Fig. 18, the absolute values of pitching moment and drag coefficient were almost the same for all the cases with minimal difference in their time history data. The formation of shock waves was not affected in these cases, but the average membrane deformation was reduced by increasing the Young's modulus. Such an increase in Young's modulus results in an increase in the oscillation amplitude and frequency, as expected, because the inertia of the model is affected by Young's modulus, as shown in Fig. 19. The peak frequency of the torus displacement for different values of Young's modulus was in the range of 73 – 84 Hz, and the amplitude tended to increase linearly. The pitching moment coefficient oscillated at approximately 30 Hz, whereas the drag coefficient peak oscillation frequency and amplitude decreased with increasing Young's modulus.

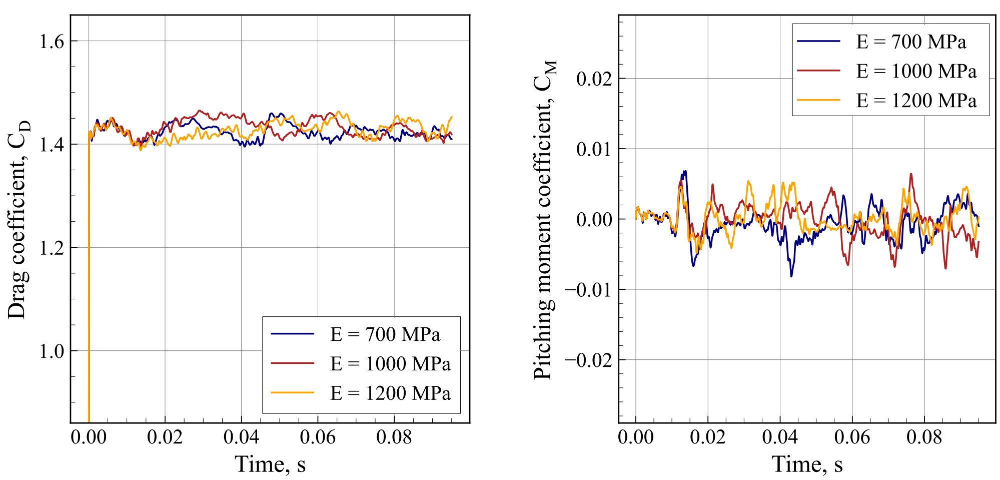

(a) Drag coefficient **(b) Pitching moment coefficient**

Fig. 18 Comparison of pitching moment and drag coefficient for different values of Young's modulus

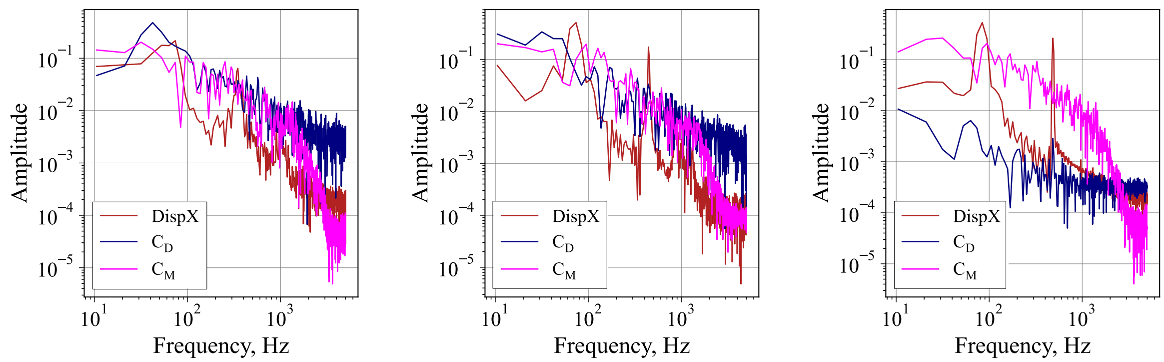

(a) E = 700 MPa **(b)** E **= 1000 MPa** **(c)** E **= 1200 MPa**

Fig. 19 Frequency-domain plot of aerodynamic coefficients for different values of Young's modulus

2. Sting Effect

For higher angles of attack, the separated flow from the inflatable torus occasionally hit the sting. To study the effect of the presence of a sting on the aerodynamic characteristics of the aeroshell, we performed a numerical analysis with and without the sting while considering the model as elastic and rigid. Rear views of the test model with and without a sting are shown in Fig. 20, and the computational mesh for the analysis is shown in Fig. 21. The computational grids were optimized such that the results were independent of the mesh size. The analyses were performed for a Mach number of 0.9 and an angle of attack of 10°. A comparison of the aerodynamic coefficients is shown in Fig. 22. The time history data shows that the pitching moment coefficient was affected most by the absence of a sting. Without sting, the pitching moment exhibited significant transient behavior compared with the case with sting. The drag coefficient appeared to be less affected by the presence or absence of a sting. However, as shown in Fig. 22 (c), the torus displacement tended to be greater without the sting. This implies that the oscillatory behavior is more significant when no sting is used. Additionally, the onset of oscillatory motion was early in this instance. The frequency-domain plots for the cases with and without the sting, considering the model to be rigid and elastic, are shown in Fig. 23. The peak frequencies of torus displacement with and without the sting were 326 and 63 Hz, respectively. However, the amplitude of the torus displacement was higher without the sting, which represents a larger oscillation for this analysis. The peak frequency of the pitching moment coefficient oscillation increased from 52 to 167 Hz when no sting was used. The formation of wrinkles on the membrane surface for the cases with and without sting is shown in Figs. 24 and 25. We observed that the sting affected the pressure distribution in the wake region, which affected the deformation of the membrane surface. Owing to the large wake created by the absence of a sting, the pressure difference between the front and rear of the vehicle increased, and an additional net force developed, leading to deeper depressions and wrinkle formation on the membrane surface.

The Mach number distributions for the cases with and without the sting are compared in Fig. 26. The deformation of the membrane surface is clearly observed, and different positions of the inflatable torus owing to oscillatory motion

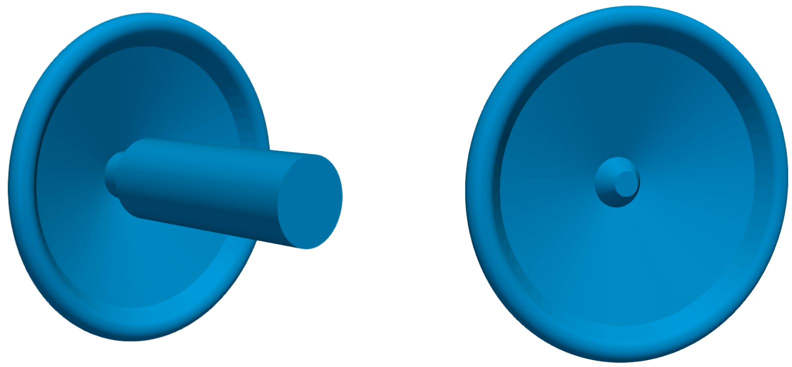

(a) With sting **(b) Without sting**

Fig. 20 Test model with and without the sting

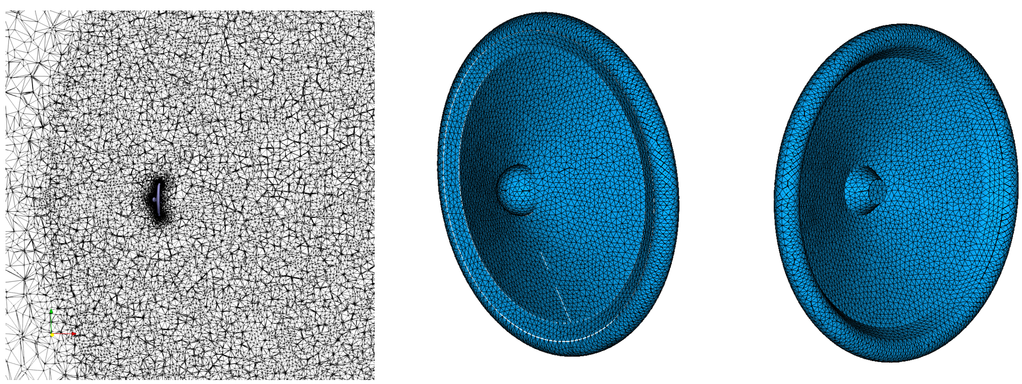

(a) SU2 mesh **(b) CCX mesh (front)** **(c) CCX mesh (back)**

Fig. 21 Computational grids used to analyze the sting effect

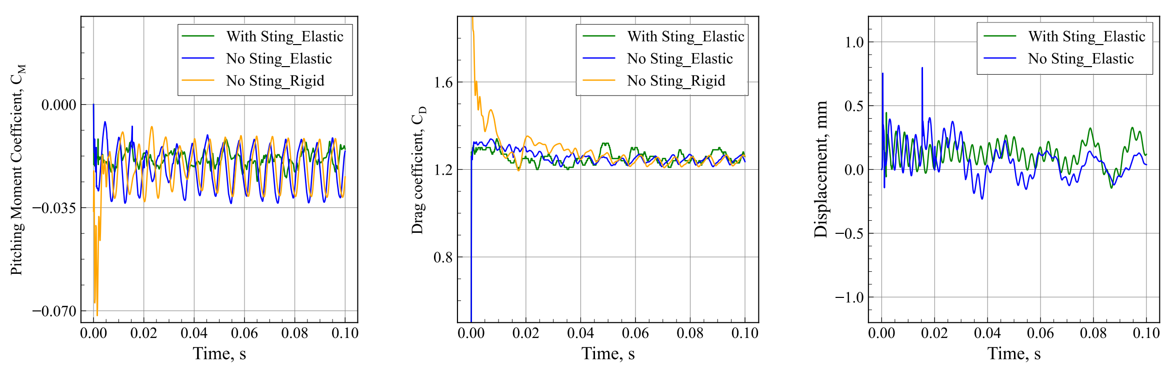

(a) Pitching moment coefficient **(b) Drag coefficient** **(c) Torus displacement**

Fig. 22 Comparison of aerodynamic coefficients for analysis model with and without the sting

can be seen in the figure. The backward flow generated in the low-pressure wake region hit the sting and formed a thin shear layer behind the vehicle. When no sting was used, the backward flow moved closer to the membrane surface, and

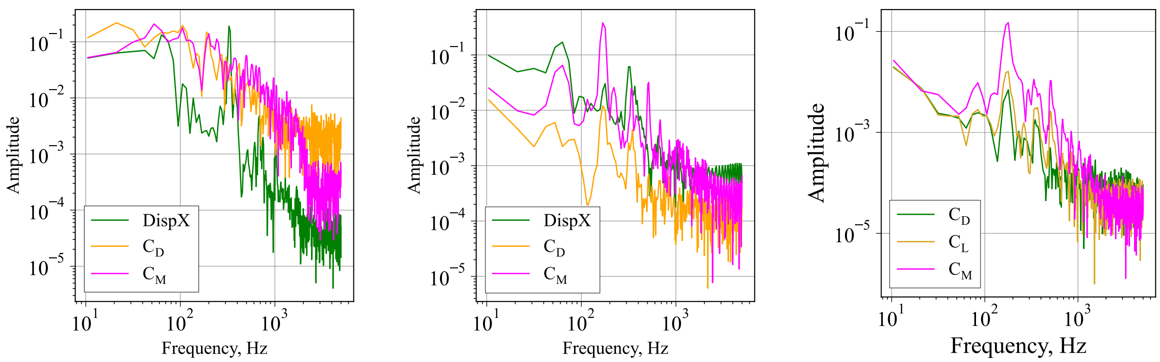

(a) Elastic (with sting) **(b) Elastic (no sting)** **(c) Rigid (no sting)**

Fig. 23 Frequency-domain plot of aerodynamic coefficients for cases with and without the sting

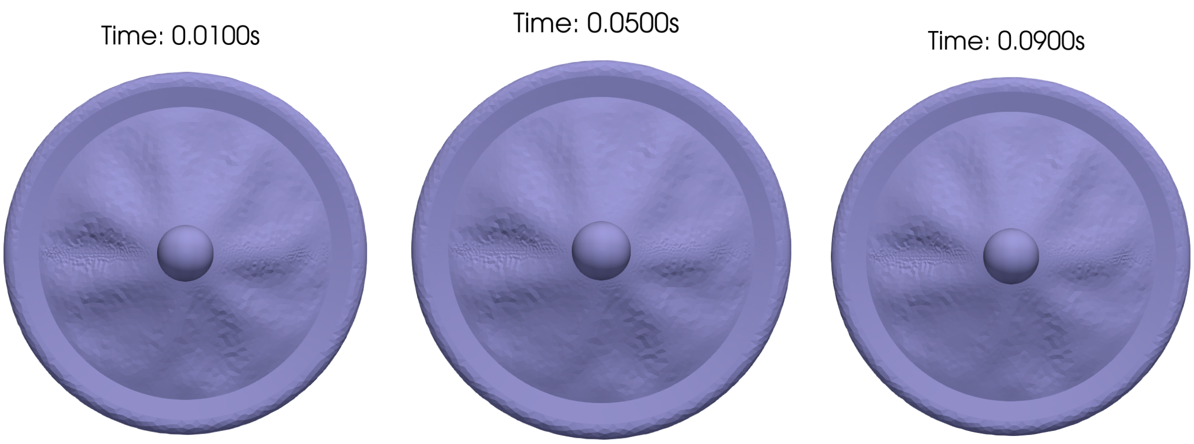

(a) Δt = 100 **(with sting)** **(b)** Δt = 500 **(with sting)** **(c)** Δt = 900 **(with sting)**

Fig. 24 Formation of membrane wrinkles for the case with a sting

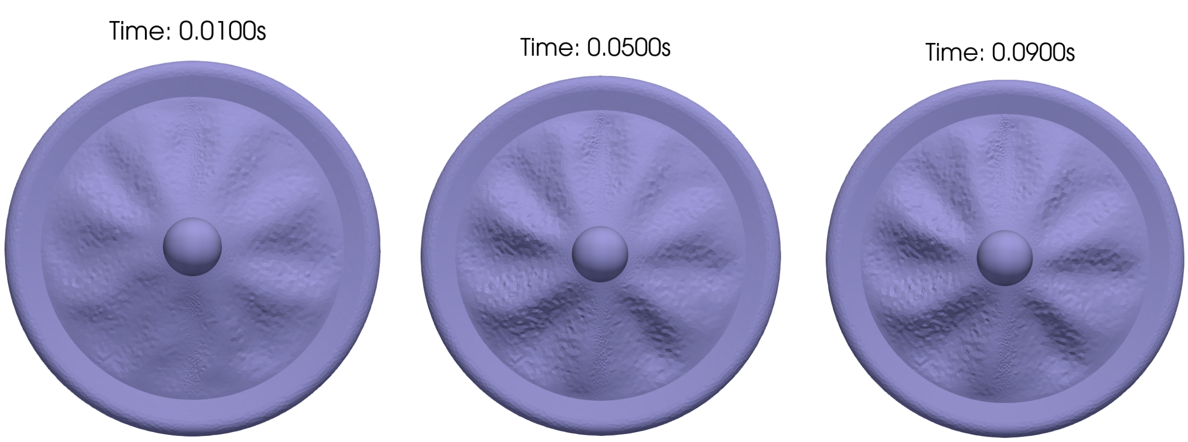

(a) Δt = 100 **(without sting)** **(b)** Δt = 500 **(without sting)** **(c)** Δt = 900 **(without sting)**

Fig. 25 Formation of membrane wrinkles in the case without the sting

a large separation vortex appeared on the rear side of the aeroshell. Continuous vortex generation and shedding led to significant transient oscillations in aerodynamics.

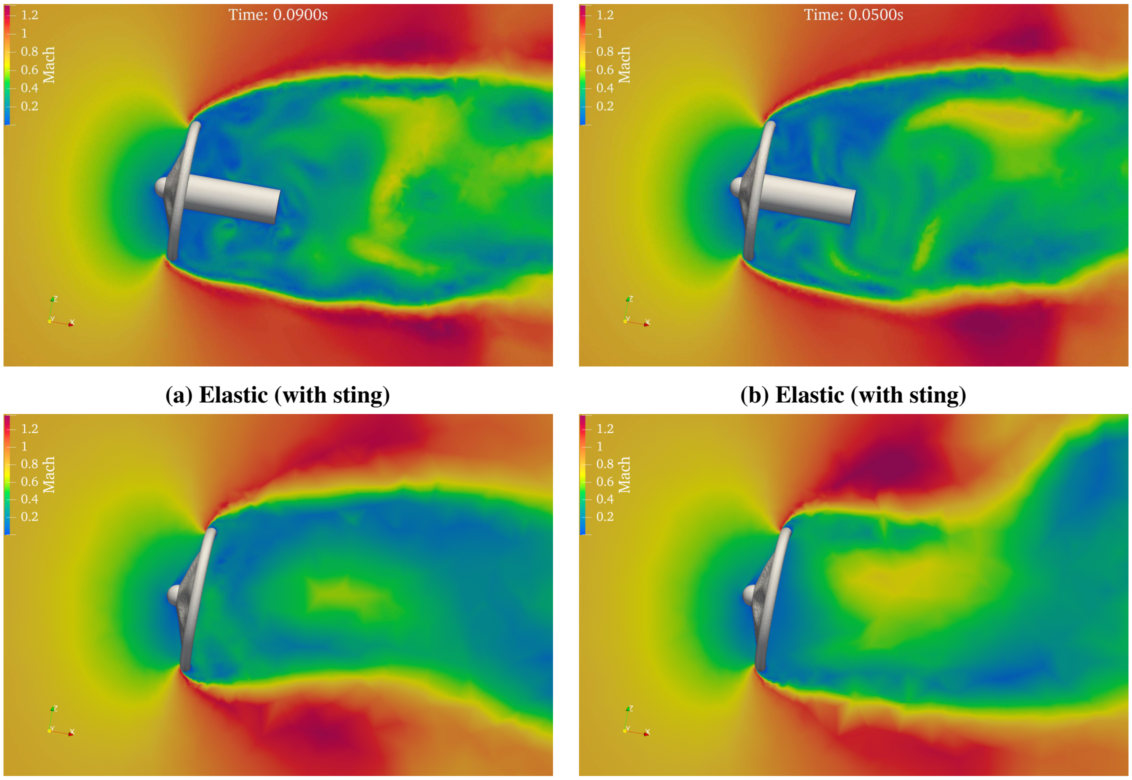

(a) Elastic (with sting) **(b) Elastic (with sting)**

(c) Elastic (no sting) **(d) Elastic (no sting)**

Fig. 26 Mach number distribution for the cases with and without the sting

3. Role of Dynamic Pressure

Dynamic pressure, which is a property of a moving fluid, is defined as the kinetic energy of a fluid per unit volume. The dynamic pressure is influenced by both local density and flow velocity. Because the fluid density varies with altitude in a complicated manner, the dynamic pressure on a reentry vehicle differs significantly. To clarify the role of the dynamic pressure of the flow on the aerodynamics and structural performance of the membrane aeroshell, we performed numerical analyses for two different dynamic pressures, 7.95 and 0.19 kPa, while fixing the freestream Mach number at 0.9 and the angle of attack at 0°.

The time history data for the pitching moment coefficient, drag coefficient, and inflatable torus displacement are shown in Fig. 27. The pitching moment coefficient exhibited a similar transient behavior for both cases of dynamic pressure. However, the average value of the pitching moment coefficient decreased with a decrease in freestream dynamic pressure. The average drag coefficient was higher at a dynamic pressure of 7.95 kPa, which is relevant because reducing the dynamic pressure can increase the freestream density. The unique features of the different dynamic

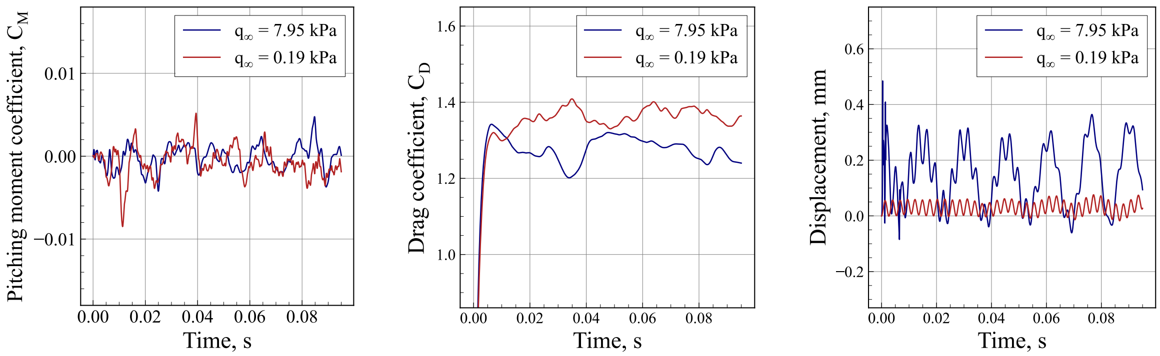

(a) Pitching moment coefficient **(b) Drag coefficient** **(c) Torus displacement**

Fig. 27 Time history data of aerodynamic coefficients for different dynamic pressures

pressures of the flow can be observed in the time history data of the inflatable torus displacement, as shown in Fig. 27(c). Lowering the dynamic pressure led to a higher frequency but a lower amplitude of oscillation. This is self-justified because the pressure difference between the front and rear of the vehicle was affected by the difference in flow density.

The frequency-domain plots of the aerodynamic coefficients and torus displacement are shown in Fig. 28. The peak frequency of torus displacement was 63 Hz at a dynamic pressure 7.95 kPa. When the freestream dynamic pressure decreases to 0.19 kPa, the frequency shifted to 368 Hz. The amplitude decreased when the dynamic pressure decreases. Therefore, the freestream dynamic pressure had a significant effect on the oscillatory behavior of the aeroshell under transonic flow conditions.

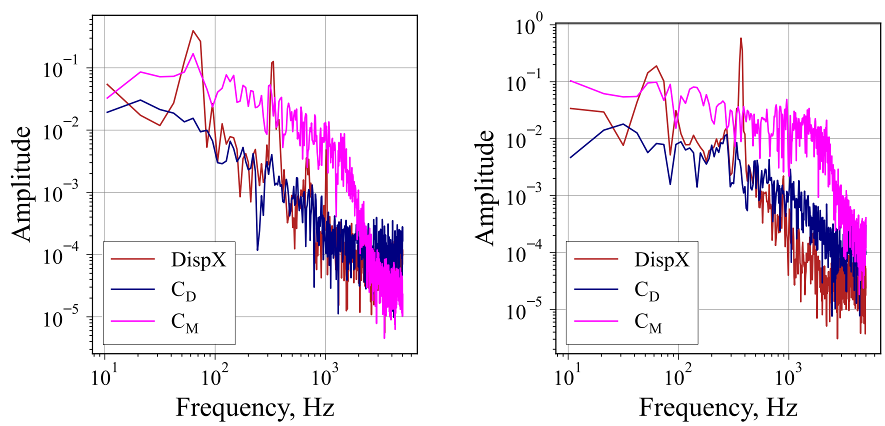

(a) q_∞ = 7.95 **kPa** **(b)** q_∞ = 0.19 **kPa**

Fig. 28 Frequency-domain plot of aerodynamic coefficients and torus displacement at different dynamic pressures

The instantaneous Mach number distributions for the different dynamic pressure cases are shown in Fig. 29. The base flow features were similar in both cases, although the oscillation behavior differed significantly. The flow separated early from the inflatable torus, and the width of the wake exceeded the maximum diameter of the aeroshell in the low

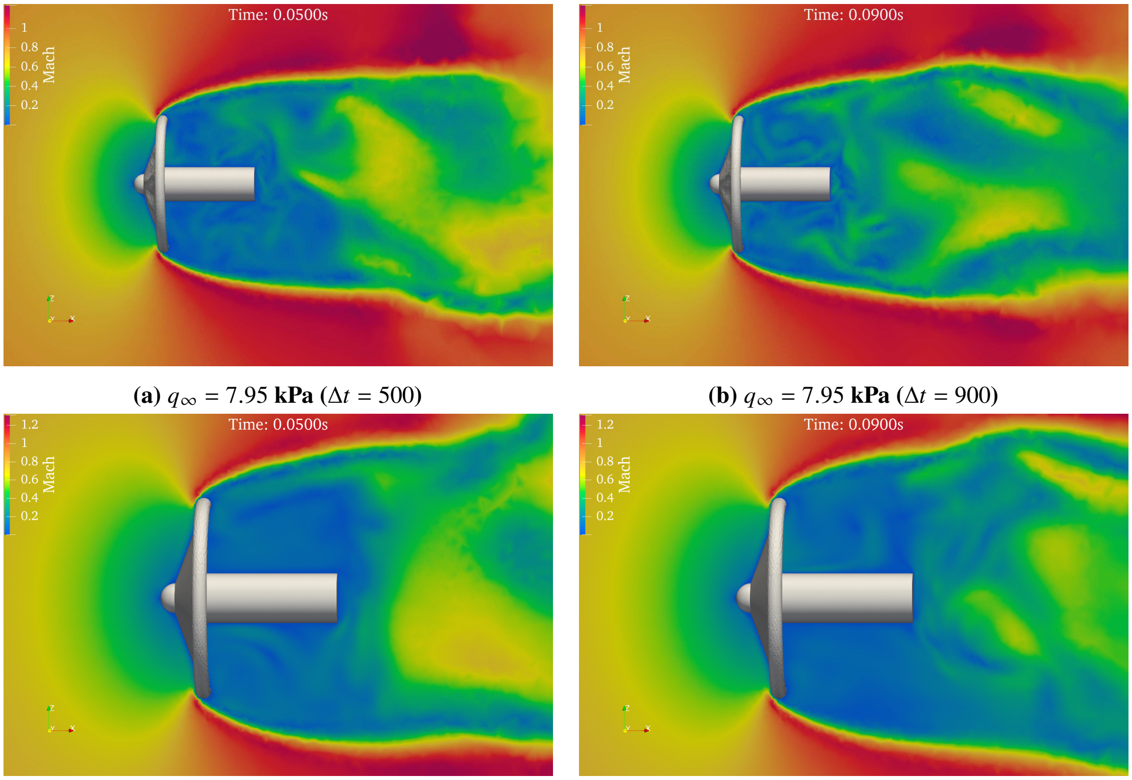

(a) q_∞ = 7.95 **kPa** (Δt = 500) **(b)** q_∞ = 7.95 **kPa** (Δt = 900)

(c) q_∞ = 0.19 **kPa** (Δt = 500) **(d)** q_∞ = 0.19 **kPa** (Δt = 900)

Fig. 29 Mach number distribution at different dynamic pressures

dynamic pressure case. The formation of wrinkles on the membrane surface was more noticeable under high dynamic pressures.

VII. Conclusion

In this study, a coupled analysis framework was developed to investigate the feedback effect of structural deformation and fluid dynamics for reentry vehicles with deployable structures based on open-source software. The analysis model was composed of an unsteady viscous and compressible fluid solver SU2 on the fluid side and a geometric nonlinear structural dynamics solver CalculiX on the structural side, coupled with the coupling library preCICE. A numerical study considering shape deformation was performed for a flexible aeroshell to evaluate the aerodynamic characteristics at transonic speeds and clarify the details of the coupled behavior of the fluid and structure. Elastic deformation of the membrane surface in high-speed airflow occurs because of aerodynamic forces manifested by frontal shock waves and backward expansion waves. In the present case, the deformation was relatively small, and no significant change in the shock wave shape was observed. The wrinkles and depressions formed exhibited transient behavior owing to the oscillatory motion of the aeroshell caused by the wake vortex in the recirculation region. The deformation of the membrane surface is affected by the Young's modulus of the material. Increasing the stiffness is a possible method of improving the structural integrity of the aeroshell. Additionally, the dynamic pressure significantly affects the oscillation characteristics of the aeroshell. This study concluded that the flexible aeroshell functioned sufficiently well to provide aerodynamic deceleration under transonic airflow conditions.

Acknowledgments

This study was supported by the JSPS KAKENHI Grant Numbers 20H02360, "Joint Usage/Research Center for Interdisciplinary Large-scale Information Infrastructures, and "High Performance Computing Infrastructure" in Japan (Project ID: jh200035, jh210029, jh220026, jh230047, and EX23706), and the use of SQUID at the Cybermedia Center, Osaka University. The authors thank Mr. Scott Selland, Sheila C. F. Langa and Mohamed Elbasyouny of Hokkaido University for their constructive advice regarding this manuscript.

References

[1] Masciarelli, J., Lin, J., Rohrschneider, R., Bartels, R., Hall, J., and Ware, J., "Ultra Lightweight Ballutes for Return to Earth from Moon," *47th AIAA/ASME/ASCE/AHS/ASC Structures, Structural Dynamics, and Materials Conference 14th AIAA/ASME/AHS Adaptive Structures Conference 7th*, 2006, p. 1698. https://doi.org/10.2514/6.2006-1698.

[2] Miller, M. J., Steinfeldt, B. A., and Braun, R. D., "Supersonic Inflatable Aerodynamic Decelerators for use on Sounding Rocket Payloads," *AIAA Atmospheric Flight Mechanics Conference*, 2014, p. 1092. https://doi.org/10.2514/6.2014-1092.

[3] Rohrschneider, R. R., and Braun, R. D., "Static aeroelastic analysis of thin-film clamped ballute for titan aerocapture," *Journal of Spacecraft and Rockets*, Vol. 45, No. 4, 2008, pp. 785–801. https://doi.org/10.2514/1.33350.

[4] Lyons, D., and Johnson, W., "Ballute aerocapture trajectories at Neptune," *AIAA Atmospheric Flight Mechanics Conference and Exhibit*, 2004, p. 5181. https://doi.org/10.2514/6.2004-5181.

[5] Muppidi, S., Tang, C. Y., Van Norman, J., and Bose, D., "Aerodynamic analysis of next generation supersonic decelerators," *32nd AIAA Applied Aerodynamics Conference*, 2014, p. 2990. https://doi.org/10.2514/6.2014-2990.

[6] Clark, I., and Adler, M., "Summary of the second high-altitude, supersonic flight dynamics test for the LDSD project," *2016 IEEE Aerospace Conference*, IEEE, 2016, pp. 1–24. https://doi.org/10.1109/AERO.2016.7500618.

[7] Olds, A., Beck, R., Bose, D. M., White, J., Edquist, K. T., Hollis, B. R., Lindell, M., Cheatwood, F., Gsell, V., and Bowden, E. L., "IRVE-3 Post-Flight Reconstruction," *AIAA Aerodynamic Decelerator Systems (ADS) Conference*, 2013, p. 1390. https://doi.org/10.2514/6.2013-1390.

[8] Mazaheri, A., "High-energy atmospheric reentry test aerothermodynamic analysis," *Journal of Spacecraft and Rockets*, Vol. 50, No. 2, 2013, pp. 270–281. https://doi.org/10.2514/1.A32407.

[9] Rohrschneider, R. R., and Braun, R. D., "Survey of ballute technology for aerocapture," *Journal of Spacecraft and Rockets*, Vol. 44, No. 1, 2007, pp. 10–23. https://doi.org/10.2514/1.19288.

[10] Wilde, D., Walther, S., Pitchadze, K., Alexsaschkin, S., Vennemann, D., and Marraffa, L., "Flight test and ISS application of the Inflatable Reentry and Descent Technology (IRDT)," *Acta Astronautica*, Vol. 51, No. 1-9, 2002, pp. 83–88. https://doi.org/10.1016/S0094-5765(02)00078-4.

[11] Bassano, E., Savino, R., Richiello, C., Russo, G., Aurigemma, R., Punzo, F., et al., "Irene-italian re-entry nacelle for microgravity experiments," *IAC Conference Proceedings*, 2011, pp. 1–8.

[12] Yamada, K., Abe, T., Suzuki, K., Honma, N., Koyama, M., Nagata, Y., Abe, D., Kimura, Y., Hayashi, A. K., and Akita, D., "Deployment and flight test of inflatable membrane aeroshell using large scientific balloon," *21st AIAA aerodynamic decelerator systems technology conference and seminar*, 2011, p. 2579. https://doi.org/10.2514/6.2011-2579.

[13] Takahashi, Y., Yamada, K., and Abe, T., "Examination of radio frequency blackout for an inflatable vehicle during atmospheric reentry," *Journal of Spacecraft and Rockets*, Vol. 51, No. 2, 2014, pp. 430–441. https://doi.org/10.2514/1.A32539.

[14] Yamada, K., "Structural Strength of Flare-type Membrane Aeroshell Supported by Inflatable Torus against Aerodynamic Force," *28th ISTS, Okinawa*, 2011.

[15] Yamada, K., Abe, T., Suzuki, K., Imamura, O., and Akita, D., "Reentry Demonstration Plan of Flare-type Membrane Aeroshell for Atmospheric Entry Vehicle using a Sounding Rocket," *21st AIAA Aerodynamic Decelerator Systems Technology Conference and Seminar*, 2011, p. 2521. https://doi.org/10.2514/6.2011-2521.

[16] Yamada, K., Nagata, Y., Abe, T., Suzuki, K., Imamura, O., and Akita, D., "Reentry demonstration of flare-type membrane aeroshell for atmospheric entry vehicle using a sounding rocket," *AIAA Aerodynamic Decelerator Systems (ADS) Conference*, 2013, p. 1388. https://doi.org/10.2514/6.2013-1388.

[17] Nagata, Y., Yamada, K., Abe, T., and Suzuki, K., "Attitude dynamics for flare-type membrane aeroshell capsule in reentry flight experiment," *AIAA Aerodynamic Decelerator Systems (ADS) Conference*, 2013, p. 1285. https://doi.org/10.2514/6.2013-1285.

[18] Takahashi, Y., Matsunaga, M., Oshima, N., and Yamada, K., "Drag behavior of inflatable reentry vehicle in transonic regime," *Journal of Spacecraft and Rockets*, Vol. 56, No. 2, 2019, pp. 577–585. https://doi.org/10.2514/1.A34069.

[19] Abe, T., "A self-consistent tension shell structure for application to aerobraking vehicle and its aerodynamic characteristics," *24th Joint Propulsion Conference*, 1988, p. 3405. https://doi.org/10.2514/6.1988-3405.

[20] Mosseev, Y., "The multipurpose integrated PC-software for structural and aeroelastic analysis of decelerators, paragliders and balloons," *14th Aerodynamic Decelerator Systems Technology Conference*, 1997, p. 1455. https://doi.org/10.2514/6.1997-1455.

[21] Bartels, R. E., Moses, R. W., Scott, R. C., Templeton, J. D., Cheatwood, F. M., Gnoffo, P. A., and Buck, G. M., "A Proposed Role of Aeroelasticity in NASA's New Exploration Vision," *International Forum on Aeroelasticity and Structural Dynamics*, 2005.

[22] Buck, G., "Testing of flexible ballutes in hypersonic wind tunnels for planetary aerocapture," *44th AIAA Aerospace Sciences Meeting and Exhibit*, 2006, p. 1319. https://doi.org/10.2514/6.2006-1319.

[23] Clark, I., Cruz, J., Hughes, M., Ware, J., Madlangbayan, A., and Braun, R., "Aerodynamic and aeroelastic characteristics of a tension cone inflatable aerodynamic decelerator," *20th AIAA Aerodynamic Decelerator Systems Technology Conference and Seminar*, 2009, p. 2967. https://doi.org/10.2514/6.2009-2967.

[24] Wang, Z., Yang, S., Liu, D., Wang, X., Mignolet, M., and Bartels, R., "Nonlinear aeroelastic analysis for a wrinkling aeroshell/ballute system," *51st AIAA/ASME/ASCE/AHS/ASC Structures, Structural Dynamics, and Materials Conference 18th AIAA/ASME/AHS Adaptive Structures Conference 12th*, 2010, p. 2879. https://doi.org/10.2514/6.2010-2879.

[25] Kramer, R., Cirak, F., and Pantano, C., "Fluid–structure interaction simulations of a tension-cone inflatable aerodynamic decelerator," *AIAA journal*, Vol. 51, No. 7, 2013, pp. 1640–1656. https://doi.org/10.2514/1.J051939.

[26] Brune, A. J., Hosder, S., and Edquist, K. T., "Uncertainty Analysis of Fluid-Structure Interaction of a Deformable Hypersonic Inflatable Aerodynamic Decelerator," *20th AIAA International Space Planes and Hypersonic Systems and Technologies Conference*, 2015, p. 3581. https://doi.org/10.2514/6.2015-3581.

[27] Brune, A. J., Hosder, S., and Edquist, K. T., "Uncertainty analysis of fluid-structure interaction of a deformable hypersonic inflatable aerodynamic decelerator," *Journal of Spacecraft and Rockets*, Vol. 53, No. 4, 2016, pp. 654–668. https://doi.org/10.2514/1.A33532.

[28] McNamara, J. J., and Friedmann, P. P., "Aeroelastic and aerothermoelastic analysis in hypersonic flow: past, present, and future," *AIAA journal*, Vol. 49, No. 6, 2011, pp. 1089–1122. https://doi.org/10.2514/1.J050882.

[29] Takizawa, K., Spielman, T., Moorman, C., and Tezduyar, T. E., "Fluid-structure interaction modeling of spacecraft parachutes for simulation-based design," *Journal of Applied Mechanics*, Vol. 79, No. 1, 2012. https://doi.org/10.1115/1.4005070.

[30] Ohashi, T., Takahashi, Y., Terashima, H., and Oshima, N., "Aerodynamic instability of flare-type membrane inflatable vehicle in suborbital reentry demonstration," *Journal of Fluid Science and Technology*, Vol. 13, No. 3, 2018, pp. JFST0020–JFST0020. https://doi.org/10.1299/jfst.2018jfst0020.

[31] Xu, J., "Structural dynamic characteristics of inflatable return vehicle," Master's thesis, Harbin Institute of Technology, Harbin, 2012.

[32] Li, L., Gonyea, K., and Braun, R. D., "Finite Element Analysis of the Inflatable Re-Entry Vehicle Experiment (IRVE)," *56th AIAA/ASCE/AHS/ASC Structures, Structural Dynamics, and Materials Conference*, 2015, p. 0204. https://doi.org/10.2514/6.2015-0204.

[33] Baginski, F., and Brakke, K., "Stability of the Axisymmetric State of a Pneumatic Envelope with Applications to Tension Cone Inflatable Aerodynamic Decelerators," *52nd AIAA/ASME/ASCE/AHS/ASC Structures, Structural Dynamics and Materials Conference 19th AIAA/ASME/AHS Adaptive Structures Conference 13t*, 2011, p. 2127. https://doi.org/10.2514/6.2011-2127.

[34] Takahashi, Y., Yamada, K., Abe, T., and Suzuki, K., "Aerodynamic heating around flare-type membrane inflatable vehicle in suborbital reentry demonstration flight," *Journal of spacecraft and rockets*, Vol. 52, No. 6, 2015, pp. 1530–1541. https://doi.org/10.2514/1.A33170.

[35] Takahashi, Y., Ha, D., Oshima, N., Yamada, K., Abe, T., and Suzuki, K., "Aerodecelerator performance of flare-type membrane inflatable vehicle in suborbital reentry," *Journal of Spacecraft and Rockets*, Vol. 54, No. 5, 2017, pp. 993–1004. https://doi.org/10.2514/1.A33682.

[36] Benra, F.-K., Dohmen, H. J., Pei, J., Schuster, S., Wan, B., et al., "A comparison of one-way and two-way coupling methods for numerical analysis of fluid-structure interactions," *Journal of applied mathematics*, Vol. 2011, 2011. https://doi.org/10.1155/2011/853560.

[37] Dasgupta, A., "A study of coupling fidelity and the aerodynamic trajectory parameters that drive static aerothermoelasticity in hypersonic flow," Ph.D. thesis, UNSW Sydney, 2018. https://doi.org/10.26190/unsworks/20764.

[38] Saha, S. K., Tobari, J., Takahashi, Y., Oshima, N., Moriyoshi, T., Yamada, K., and Shibata, R., "Fluid-structure interaction characteristics of inflatable reentry aeroshell at subsonic speed," *Aerospace Science and Technology*, Vol. 133, 2023, p. 108112. https://doi.org/10.1016/j.ast.2023.108112.

[39] Wu, J., Zhang, Z., Hou, A., Xue, X., and Cao, X., "Thermal Aeroelastic Characteristics of Inflatable Reentry Vehicle Experiment (IRVE) in Hypersonic Flow," *International Journal of Aerospace Engineering*, Vol. 2021, 2021. https://doi.org/10.1155/2021/6673818.

[40] Economon, T. D., Palacios, F., Copeland, S. R., Lukaczyk, T. W., and Alonso, J. J., "SU2: An open-source suite for multiphysics simulation and design," *Aiaa Journal*, Vol. 54, No. 3, 2016, pp. 828–846. https://doi.org/10.2514/1.J053813.

[41] Dhondt, G., and Wittig, K., "Calculix: a free software three-dimensional structural finite element program," *MTU Aero Engines GmbH, Munich*, 1998.

[42] Bungartz, H.-J., Lindner, F., Gatzhammer, B., Mehl, M., Scheufele, K., Shukaev, A., and Uekermann, B., "preCICE–a fully parallel library for multi-physics surface coupling," *Computers & Fluids*, Vol. 141, 2016, pp. 250–258. https://doi.org/10.1016/j.compfluid.2016.04.003.

[43] Degroote, J., Bruggeman, P., Haelterman, R., and Vierendeels, J., "Stability of a coupling technique for partitioned solvers in FSI applications," *Computers & Structures*, Vol. 86, No. 23-24, 2008, pp. 2224–2234. https://doi.org/10.1016/j.compstruc.2008.05.005.

[44] Jameson, A., "Origins and further development of the Jameson–Schmidt–Turkel scheme," *AIAA Journal*, Vol. 55, No. 5, 2017, pp. 1487–1510. https://doi.org/10.2514/1.J055493.

[45] Miranda, I., Ferencz, R. M., and Hughes, T. J., "An improved implicit-explicit time integration method for structural dynamics," *Earthquake engineering & structural dynamics*, Vol. 18, No. 5, 1989, pp. 643–653. https://doi.org/10.1002/eqe.4290180505.

[46] TOYOBO CO., L., "ZYLON (PBO fiber) Technical Information," , 2005. URL https://www.toyobo-global.com/seihin/kc/pbo/zylon-p/bussei-p/technical_201118.pdf, last accessed: 2022-11-28.